JOURNAL OF SPACECRAFT AND ROCKETS
Vol. 37, No. 1, January–February 2000

Tether Deployment and Trajectory Modeling for Space Plasma Science Missions

F. R. Vigneron* and F. Schultz†
Carleton University, Ottawa, Ontario K1S 5B6, Canada
A. M. Jablonski‡
Canadian Space Agency, Ottawa, Ontario K1L 8E3, Canada
and
G. Tyc§
Bristol Aerospace, Ltd., Winnipeg, Manitoba R3L 2S4, Canada

Certain space plasma science missions employ a research payload that comprises two subpayloads that are connected by an electrically conductive tether of up to 1200 m in length. The missions are conducted in suborbital trajectory attained with a small multistage launch vehicle. A reel-type deployer is used, and subpayload separation is achieved mainly by thrusters on one of the subpayloads. The focus is on modeling the deployment phases and the orientation of the configuration in space. The subpayloads are modeled as mass points in inertial space in the Earth's gravity field. Approximate solutions are derived that provide functional relationships that are useful for mission design. Results from simulation and the approximate formulas are shown to compare well with flight dynamics measurements made with a tether force sensor and star cameras during a mission in November 1995.

Nomenclature

a, b	= superscripts or subscripts for aft and forward payload, respectively
$[\boldsymbol{c}]$, $\boldsymbol{c}_i$	= subpayloads basis and corresponding unit vectors
F^b	= thruster force matrix on body b, $\{F_1, 0, 0\}^T$, N
$\boldsymbol{F}^b$	= thruster force vector on body b, N
$\boldsymbol{F}^{ga}$, $\boldsymbol{F}^{gb}$	= gravitational force vectors on mass points, N
G_{mb}	= magnetic hysteresis brake detent torque, N-m
I_0, I_d	= moment of inertia values of reel (see Table 1), kg-m^2
$I(\theta)$	= moment of inertia of reel and wound tether about rotation axis, kg-m^2
$[\boldsymbol{i}]$, $\boldsymbol{i}_i$	= inertial basis and corresponding unit vectors
K	= spring constant of separation spring, N/m
L_f	= tether length at end of deployment, m
$L(\theta)$	= tether length variable (unstrained), m
m_a, m_b	= mass of aft and forward payloads, kg
m_e	= effective mass, $m_a m_b/(m_a + m_b)$, kg
$m_t(\theta)$, m_{t0}	= mass of tether on reel as a function of θ, and its initial value, kg
n	= matrix of components of $\boldsymbol{n}$ in $[\boldsymbol{c}]$ basis, $\{n_1, n_2, n_3\}^T$
$\boldsymbol{n}$	= unit vector along $\boldsymbol{R}$
$p(t)$	= linear momentum relative to the mass center, kg-m/s
$Q(\alpha, \beta)$	= transformation matrix from $[\boldsymbol{i}]$ to $[\boldsymbol{c}]$
$\boldsymbol{R}$	= position vector of center of mass, km
R_{cm}	= scalar magnitude of $\boldsymbol{R}$, km
R_1, R_2, R_3	= components of $\boldsymbol{R}$ in $[\boldsymbol{i}]$ basis, km
$\boldsymbol{R}^a$, $\boldsymbol{R}^b$	= position vectors of aft and forward masses
r	= matrix of separation vector resolved in $[\boldsymbol{c}]$ basis, $\{r_1, 0, 0\}^T$, m
$\boldsymbol{r}$	= separation vector between mass points, $\boldsymbol{r}^b - \boldsymbol{r}^a$, m
$\dot{r}_{10}^a$, $\dot{r}_{10}^b$	= velocities of subpayloads at time t_0 (just after spring impulse), m/s
$\boldsymbol{r}^a$, $\boldsymbol{r}^b$	= vectors from mass center to mass points a and b, m
T	= tether tension matrix, $\{T_1, 0, 0\}^T$, N
$\boldsymbol{T}$	= tether tension vector, N
t_s	= time at tether severance, s
t_0	= time at subpayload separation (after spring release), s
t_1	= time at end of thruster firing, s
U_s	= strain energy in separation spring, N-m
z_f, z_m	= reel radii, full deployment and mean value, m
z_0, z_d	= radius parameters of reel (see Table 1), m
$z(\theta)$	= reel radius variable, m
α, δ	= right ascension and declination of separation vector (Fig. 5)
β	= angle between $\boldsymbol{R}$ (or $\boldsymbol{n}$) and $\boldsymbol{r}$
Δ	= displacement of separation spring, m
θ, θ_d	= reel turn angles (see Table 1), rad
λ	= separation parameter in Eq. (59), 1/s
μ	= gravitational constant, 398,601 km^3/s^2
ω, ω_i	= angular velocity matrix, and components resolved in $[\boldsymbol{c}]$ basis, rad/s
$\boldsymbol{\omega}$	= angular velocity of $[\boldsymbol{c}]$ relative to $[\boldsymbol{i}]$, rad/s
$^\circ$	= vector differentiation viewed from $[\boldsymbol{i}]$

Introduction

CERTAIN space plasma missions employ a science payload that comprises two subpayloads that are connected by an electrically conductive tether. A mission of this type is conducted in a suborbital trajectory that is attained with a small multistage launch vehicle. Examples are the OEDIPUS A and C missions[1,2] (the acronym OEDIPUS is derived from Observation of Electric Field Distribution in Ionospheric Plasma, a Unique Strategy) and the NASA CHARGE missions.[3] Of these missions, the OEDIPUS C in 1995 was the most extensive in terms of science instruments, mission complexity and duration, apogee height, and tether length. Because the mission included tether development as part of its objective,[4] the payload was well instrumented for monitoring of tether operations.

The mission profile of OEDIPUS C is shown in Fig. 1. The payload, comprising two rocket subpayloads and a connecting tether, is shown in various stages of evolution in Fig. 1. The launcher was a Black Brant 12 launch vehicle, and the launch site was located at Poker Flats, Alaska. The suborbital trajectory of the mass center had

Presented as Paper 98-4553 at the AIAA/AAS Astrodynamics Specialist Conference and Exhibit, Boston, MA, 10–12 August 1998; received 10 January 1999; revision received 16 June 1999; accepted for publication 25 June 1999.

*Professor (Adjunct), Department of Mechanical and Aerospace Engineering. Senior Member AIAA.
†Graduate Student, Department of Mechanical and Aerospace Engineering.
‡Research Scientist, Space Science Program. Member AIAA.
§Senior Engineer, Space Business Group. Member AIAA.

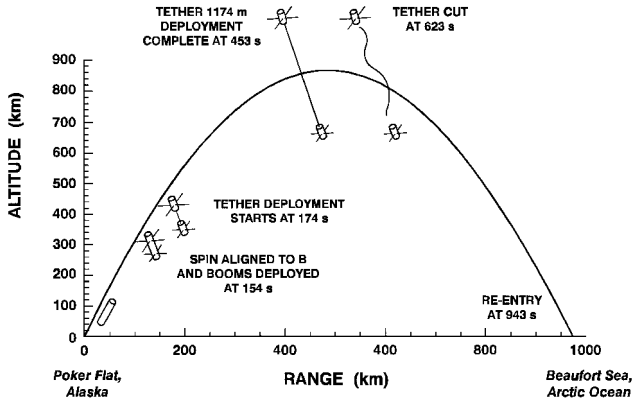

Fig. 1 Phases of the OEDIPUS-C mission.

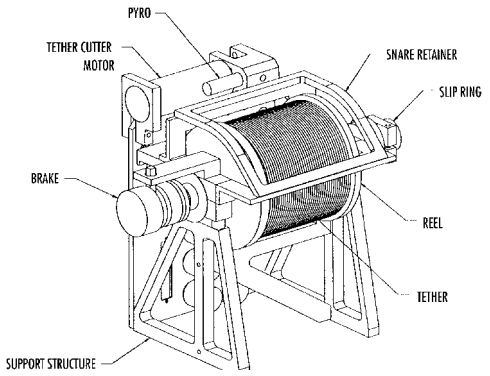

Fig. 2 OEDIPUS-C reel-type deployer.

an altitude at apogee of about 824 km, and the payload impacted Earth in the Beaufort Sea of the Arctic Ocean. In the initial stages of the mission, the two subpayloads were connected and were ejected from the launch vehicle with spin stabilization about the longitudinal axis. Eight booms were then deployed. Subpayload separation was then initiated by payload pyrotechnics and the action of a payload separation pushoff spring. Cold gas thrusters on the forward payload were activated immediately and were fired for 14.7 s; they were the main source of impulse for separation. During separation, an electrically conductive 1-mm-diam tether was deployed from a reel deployer to a length of 1174 m. The reel deployer is shown in Fig. 2. The reel has a magnetic hysteresis brake that prevents reel rotation if tether-induced torque is less that a detent value of 0.0512 N-m and that slips and applies a constant retarding reel torque if tether-induced torque equals or exceeds 0.0512 N-m. During tether deployment, the reel torque was essentially constant, the radius of the stowed tether decreased from 0.0579 to about 0.03 m, and the tether tension increased from approximately 0.5 to 1.1 N. After separation was complete the tension dropped to a lower value, and the magnetic hysteresis brake prevented further reel rotation. During the flight, the orientation of the configuration changed slowly due to the gravity gradient on the very large configuration. The tether was severed for the postapogee part of the trajectory. Comprehensive flight dynamics data were acquired during the mission, including tether force sensor data and a video taken with a camera mounted on the aft payload.

The OEDIPUS missions have demonstrated several elements of tether technology that are relevant to future space missions that may consider tethers. Specific elements are the simple reel type of deployer with magnetic hysteresis brake, the conductive tether, the use of a thruster as a main source of separation impulse for deployment, the spin stabilization in conjunction with tethers, and the tether severing devices.

The dynamics of this type mission is very complex, and the creation of a single comprehensive computer model is neither the efficient nor the practical way to support mission design and sizing of the numerous deployment and stabilization elements. For OEDIPUS, the modeling was developed in two broad categories: 1) idealization of the payloads as mass points and analysis of deployment, separation, and changes in orientation, and 2) spin stabilization dynamics of the configuration about the line joining the mass centers of the end bodies.[5–7] This paper relates to the first of these two categories; it describes model formulation and design laws and compares modeling results with OEDIPUS-C flight data.[8,9]

Trajectory and Deployment Formulation

In this section, the basic kinematic and kinetic relationships for the trajectory, tether, and reel are derived. The vector algebra convention described in Ref. 10 is used. Notation similar to that of Ref. 11 is adopted. A square-bracketed boldface symbol (e.g., $[\boldsymbol{c}]$) denotes a vector basis (vectrix). A boldface symbol refers to a vector (e.g., $\boldsymbol{R}$); its corresponding 3×1 column matrix is denoted by the same symbol without boldface (e.g., R); and the corresponding scalar components of the matrix are denoted by the same symbol with a subscript (e.g., R_1, R_2, R_3). Any special designation to a vector is indicated with a superscript (e.g., $\boldsymbol{R}^a$ refers to the aft payload). The tilde on top of a column matrix indicates the skew symmetric 3×3 matrix associated with the vector cross product. Designations to ordinary scalar (nonvector) parameters are made with subscripts (e.g., m_a denotes the mass of the aft payload).

Vector Equations of Motion of Mass Points

The subpayloads are shown in Figs. 3 and 4 relative to a geocentric reference basis $[\boldsymbol{i}]$, where $\boldsymbol{i}_1$ is in the direction of Aries and $\boldsymbol{i}_3$ is along the Earth's north pole. The subpayloads are idealized as mass points, with the aft and forward payloads having masses m_a and m_b, respectively. The tether is shown as partially deployed, and the mass of the deployed portion is assumed negligible relative to the subpayloads. The force balance for the subpayloads is shown in Fig. 4:

$$m_a \ddot{\boldsymbol{R}}^a = \boldsymbol{F}^{ga} + \boldsymbol{T} \tag{1}$$

$$m_b \ddot{\boldsymbol{R}}^b = \boldsymbol{F}^{gb} - \boldsymbol{T} + \boldsymbol{F}^b \tag{2}$$

From Fig. 3,

$$\boldsymbol{R}^a = \boldsymbol{R} + \boldsymbol{r}^a \tag{3}$$

$$\boldsymbol{R}^b = \boldsymbol{R} + \boldsymbol{r}^b \tag{4}$$

$\boldsymbol{r}^a$ and $\boldsymbol{r}^b$ are referenced from the center of mass and, thus,

$$m_a \boldsymbol{r}^a + m_b \boldsymbol{r}^b = \boldsymbol{0} \tag{5}$$

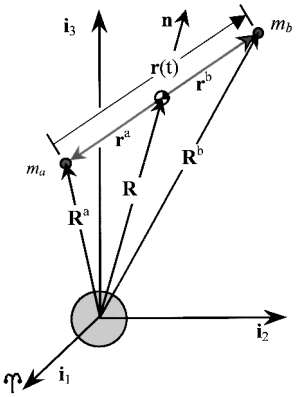

Fig. 3 Position and separation vectors.

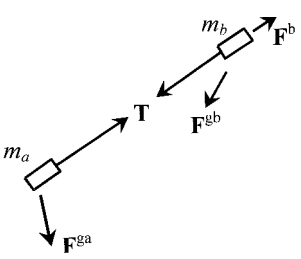

Fig. 4 Forces on mass points.

The gravitational force can be derived in the form of a series expansion in terms of products $(\boldsymbol{r}\cdot\boldsymbol{R})/(\boldsymbol{R}\cdot\boldsymbol{R})$ to third order and is

$$\boldsymbol{F}^{gi} = -\left(\mu m_i \middle| \; R_{\rm cm}^3\right)\boldsymbol{R} + \left(\mu m_i \middle| \; R_{\rm cm}^3\right)\{3(\boldsymbol{n}\cdot\boldsymbol{r}^i)\boldsymbol{n} - \boldsymbol{r}^i\} \quad (6)$$

where $i = a$ or b. In Eq. (6), $R_{\rm cm} = \sqrt{(\boldsymbol{R}\cdot\boldsymbol{R})}$, and $\boldsymbol{n}$ is the unit vector along the trajectory radius, that is, $\boldsymbol{n} = \boldsymbol{R}/R_{\rm cm}$. Substitution of Eqs. (3), (4), and (6) into Eq. (1) leads to

$$m_a\ddot{\boldsymbol{R}} + m_a\ddot{\boldsymbol{r}}^a = -\left(\mu m_a \middle| \; R_{\rm cm}^3\right)\boldsymbol{R} + \left(\mu m_a \middle| \; R_{\rm cm}^3\right)\{3(\boldsymbol{n}\cdot\boldsymbol{r}^a)\cdot\boldsymbol{n} - \boldsymbol{r}^a\} + \boldsymbol{T} \quad (7)$$

Similarly, Eq. (2) becomes

$$m_a\ddot{\boldsymbol{R}} + m_a\ddot{\boldsymbol{r}}^b = -\left(\mu m_b \middle| \; R_{\rm cm}^3\right)\boldsymbol{R} + \left(\mu m_b \middle| \; R_{\rm cm}^3\right)\{3(\boldsymbol{n}\cdot\boldsymbol{r}^b)\cdot\boldsymbol{n} - \boldsymbol{r}^b\} - \boldsymbol{T} + \boldsymbol{F}^b \quad (8)$$

Trajectory of the Mass Center

Addition of Eqs. (7) and (8) and use of Eq. (5) results in

$$(m_a + m_b)\ddot{\boldsymbol{R}} = -\frac{\mu(m_a + m_b)}{R_{\rm cm}^3}\boldsymbol{R} + \boldsymbol{F}^b \quad (9)$$

Equation (9) provides for the calculation of the trajectory of the mass center. Equation (9) is uncoupled from $\boldsymbol{r}^a$ and $\boldsymbol{r}^b$, and thus $\boldsymbol{R}$ and $\boldsymbol{n}$ may be determined separately from deployment dynamics. For preflight analysis, $\boldsymbol{R}$ may be calculated by standard methods, given the trajectory parameters of the mission. For OEDIPUS C, tracking data were also available after flight, from which $\boldsymbol{R}$ could be deduced directly. OEDIPUS C was in a near-polar suborbital elliptical trajectory, with apoapsis of 7184 km (apogee altitude of 824 km) and periapsis of 106.5 km (the suborbital elliptical trajectory intersects the Earth). The flight time was approximately 18 min.

Separation Vector

Divide Eq. (9) by $m_a + m_b$ and combine the result with Eq. (8) to obtain

$$m_b\ddot{\boldsymbol{r}}^b = \left(\mu m_\beta \middle| \; R_{\rm cm}^3\right)\{3(\boldsymbol{n}\cdot\boldsymbol{r}^b)\boldsymbol{n} - \boldsymbol{r}^b\} - \boldsymbol{T} + [m_a/(m_a + m_b)]\boldsymbol{F}^b \quad (10)$$

The separation vector $\boldsymbol{r}$ between the two payloads is shown in Fig. 3 and is

$$\boldsymbol{r} = \boldsymbol{r}^b - \boldsymbol{r}^a \quad (11)$$

Combine Eq. (11) with Eq. (5):

$$\boldsymbol{r}^b = [m_a/(m_a + m_b)]\boldsymbol{r} \quad (12)$$

Substitution of Eq. (12) into Eq. (10) then leads to the following differential equation for the separation vector:

$$m_e\ddot{\boldsymbol{r}} = \left(\mu m_e \middle| \; R_{\rm cm}^3\right)\{3(\boldsymbol{n}\cdot\boldsymbol{r})\boldsymbol{n} - \boldsymbol{r}\} - \boldsymbol{T} + (m_e/m_b)\boldsymbol{F}^b \quad (13)$$

where m_e is the effective mass:

$$m_e = m_a m_b/(m_a + m_b) \quad (14)$$

Equation (13) provides for the calculation of $\boldsymbol{r}$ and regards $\boldsymbol{R}$ and $\boldsymbol{n}$ as input functions as described earlier.

Separation Vector in Right Ascension and Declination Variables

The most convenient scalars to describe $\boldsymbol{r}$ in the tethered payload application are the separation distance measured along the line joining the two mass points $|\boldsymbol{r}|$ and the declination δ and right ascension α of the separation vector as measured relative to the inertial basis $[\boldsymbol{i}]$. This choice leads to equations that are compatible with a model of the reel deployer and also with flight data from subpayload-mounted star trackers[7,8] and the tether force sensor.[9]

The subpayloads $[\boldsymbol{c}]$ basis is defined relative to the inertial $[\boldsymbol{i}]$ basis by 1) a rotation about $\boldsymbol{i}_3$ by angle α, leading to the $[\boldsymbol{i}']$ basis, where

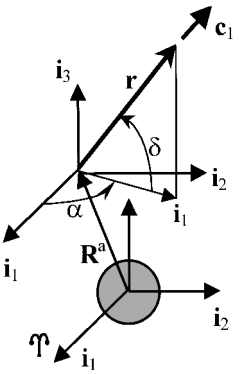

Fig. 5 Right ascension and declination variables.

$\boldsymbol{i}_1$, $\boldsymbol{r}$, and $\boldsymbol{i}_3'$ are coplanar, and 2) an additional rotation about $\boldsymbol{i}_2'$ by an angle δ in the negative $\boldsymbol{i}_2'$ direction, to arrive at the $[\boldsymbol{c}]$ basis, where $\boldsymbol{c}_1$ is aligned along $\boldsymbol{r}$, the separation vector. The transformation is shown in Fig. 5. It is

$$[\boldsymbol{c}] = Q[\boldsymbol{i}] \quad (15)$$

where Q is the orthonormal matrix:

$$Q(\alpha,\delta) = \begin{bmatrix} \cos\delta\cos\alpha & \cos\delta\sin\alpha & \sin\delta \\ -\sin\alpha & \cos\alpha & 0 \\ -\sin\delta\cos\alpha & -\sin\delta\cos\alpha & \cos\delta \end{bmatrix} \quad (16)$$

The angular velocity of $[\boldsymbol{c}]$ relative to $[\boldsymbol{i}]$ is

$$\omega = [\boldsymbol{c}]^T\omega = [\boldsymbol{c}]^T\begin{Bmatrix}\omega_1\\ \omega_2\\ \omega_3\end{Bmatrix} \quad (17)$$

where

$$\omega_1 = \dot{\alpha}\sin\delta, \qquad \omega_2 = -\dot{\delta}, \qquad \omega_3 = \dot{\alpha}\cos\delta \quad (18)$$

The components ω_1 and ω_3 are not independent. By combining the first and last elements of Eq. (18),

$$\omega_1 = \omega_3\tan\delta \quad (19)$$

The inverse of Eq. (18) is, thus,

$$\dot{\delta} = -\omega_2 \quad (20)$$

$$\dot{\alpha} = \omega_3/\cos\delta \quad (21)$$

The resolution of $\boldsymbol{r}$ in the $[\boldsymbol{c}]$ basis has the form

$$\boldsymbol{r} = [\boldsymbol{c}]^T r \quad (22)$$

and $r = \{r_1, 0, 0\}^T$ because $\boldsymbol{c}_1$ lies along the separation vector. The separation distance between the two mass points is, thus, described by the scalar variable $r_1(t)$. Likewise, the vectors $\boldsymbol{T}$ and $\boldsymbol{F}^b$ have the following component forms:

$$\boldsymbol{T} = [\boldsymbol{c}]^T T, \qquad \boldsymbol{F}^b = [\boldsymbol{c}]^T F^b \quad (23)$$

where $T = \{T_1, 0, 0\}^T$ and $F^b = \{F_1^b, 0, 0\}^T$. The natural basis in which to resolve $\boldsymbol{R}$ is $[\boldsymbol{i}]$, that is,

$$\boldsymbol{R} = [\boldsymbol{i}]^T R \quad (24)$$

where $R = \{R_1, R_2, R_3\}^T$. Then $\boldsymbol{n}$ is

$$\boldsymbol{n} = [\boldsymbol{i}]^T\begin{Bmatrix} R_1/R_{\rm cm}\\ R_2/R_{\rm cm}\\ R_3/R_{\rm cm}\end{Bmatrix} \quad (25)$$

It is also convenient to define components of $\boldsymbol{n}$ in the $[\boldsymbol{c}]$ basis:

$$\boldsymbol{n} = [\boldsymbol{c}]^T n \quad (26)$$

where $n = \{n_1, n_2, n_3\}^T$. Equation (15) may be reconfigured as $[\boldsymbol{i}]^T = [\boldsymbol{c}]^T Q$, and then it follows from Eqs. (25) and (26) that

$$n = \begin{Bmatrix} n_1 \\ n_2 \\ n_3 \end{Bmatrix} = Q \begin{Bmatrix} R_1/R_{\rm cm} \\ R_2/R_{\rm cm} \\ R_3/R_{\rm cm} \end{Bmatrix} \tag{27}$$

The next step is to obtain the matrix form of Eq. (13) resolved in the $[\boldsymbol{c}]$ basis. The vector differential $\ddot{\boldsymbol{r}}$ resolves to $\ddot{\boldsymbol{r}} = [\boldsymbol{c}]^T(\ddot{r} + \dot{\tilde{\omega}} r + 2\tilde{\omega}\dot{r} + \tilde{\omega}\tilde{\omega} r)$. Substitution of the foregoing plus Eqs. (26), (22), and (23) into Eq.(13) gives the intermediate result

$$\ddot{r} + \dot{\tilde{\omega}} r + 2\tilde{\omega}\dot{r} + \tilde{\omega}\tilde{\omega} r = \left(\mu \middle| R_{\rm cm}^3\right)\{3(r^T n)n - r\}$$

$$-(1/m_e)T + (1/m_b)F^b \tag{28}$$

In Eq. (28), $\tilde{\omega}$ is

$$\tilde{\omega} = \begin{bmatrix} 0 & -\omega_3 & \omega_2 \\ \omega_3 & 0 & -\omega_1 \\ -\omega_2 & \omega_1 & 0 \end{bmatrix} \tag{29}$$

Reduction of Eq. (28) to scalar component form results in the following key equations:

$$\ddot{r}_1 = \left\{\left(\mu \middle| R_{\rm cm}^3\right)\left(3n_1^2 - 1\right) + \omega_2^2 + \omega_3^2\right\} r_1 - T_1/m_e + F_1^b \middle| m_b \tag{30a}$$

$$\dot{\omega}_3 + 2(\dot{r}_1/r_1)\omega_3 + \omega_2\omega_3 \tan\delta = 3\left(\mu \middle| R_{\rm cm}^3\right) n_1 n_2 \tag{30b}$$

$$\dot{\omega}_2 + 2(\dot{r}_1/r_1)\omega_2 + \omega_3^2 \tan\delta = -3\left(\mu \middle| R_{\rm cm}^3\right) n_1 n_3 \tag{30c}$$

Initial Velocity Imparted by the Separation Spring

The action of the separation spring between the two payloads may be modeled as an impulse that imparts an initial velocity condition on the separation variable $\dot{r}_1(t)$ at the time t_0. Consider the incremental dynamics of the subpayloads along the separation $\boldsymbol{c}_1$ direction. With reference to Figs. 3 and 5, $\boldsymbol{r}^b(t) = [\boldsymbol{c}]^T\{r_1^b(t), 0, 0\}^T$ and $\boldsymbol{r}^a(t) = -[\boldsymbol{c}]^T\{r_1^a(t), 0, 0\}^T$. The separation vector is $\boldsymbol{r}(t) = [\boldsymbol{c}]^T\{r_1(t), 0, 0\}^T$. Therefore,

$$r_1(t) = r_1^b(t) - r_1^a(t) \tag{31}$$

The linear momentum of the two subpayloads relative to the mass center is in the $\boldsymbol{c}_1$ direction, and its scalar magnitude is

$$p(t) = m_b \dot{r}_1^b(t) - m_a \dot{r}_1^a(t) \tag{32}$$

Linear momentum is conserved over the impulsive spring release. Immediately before spring release and subpayload separation, $\dot{r}_1^a$ and $\dot{r}_1^b$ are zero and, thus, $p = 0$. At time t_0, which is immediately after the impulsive spring release, linear momentum is $m_b \dot{r}_{10}^b - m_a \dot{r}_{10}^a$. Hence,

$$m_b \dot{r}_{10}^b - m_a \dot{r}_{10}^a = 0 \tag{33}$$

The total energy (kinetic plus potential energy) is also assumed conserved over the impulsive spring release. Before release the kinetic energy is zero, and the potential energy is the spring's strain energy $U_s = \frac{1}{2} K \Delta^2$. After spring release, the strain energy is zero, and the kinetic energy is $\frac{1}{2} m_b (\dot{r}_{10}^b)^2 + \frac{1}{2} m_a (\dot{r}_{10}^a)^2$. Hence,

$$\tfrac{1}{2} m_b \left(\dot{r}_{10}^b\right)^2 + \tfrac{1}{2} m_a \left(\dot{r}_{10}^a\right)^2 = U_s \tag{34}$$

Equations (33) and (34) may be solved for the subpayload velocities:

$$\left(\dot{r}_{10}^a\right)^2 = 2m_e U_s^2 \middle| m_a^2, \qquad \left(\dot{r}_{10}^b\right)^2 = 2m_e U_s^2 \middle| m_b^2 \tag{35}$$

where $m_e = m_a m_b/(m_a + m_b)$. Equation (31) may be squared to give $\dot{r}_{10}^2 = \dot{r}_{10}^{a2} + \dot{r}_{10}^{b2} + 2\dot{r}_{10}^a \dot{r}_{10}^b$. Combination with Eq. (35) yields the formula for the initial condition at time t_0:

$$\dot{r}_{10}(t_0) = \sqrt{2U_s/m_e} \tag{36}$$

Deployer

The reel type of deployer is shown in Fig. 2. It consists of a reel, a magnetic hysteresis brake, and a stored tether. In flight, the tether is pulled off the reel by the tension initiated by the payload separation spring and thrusters.

Kinematics

Before flight, the tether is very carefully wound on to the reel, and the relationship of reel turn angle θ to reel radius z and unstored length L is recorded. A detailed computer model of the layer-by-layer deployment that generates $z(\theta)$ and $L(\theta)$ was developed. A simpler approximate analytical model that is suited for algebraic analysis is described here. The measured radius data were noted in test data to be a linear function of the measured reel rotation angle (to first order), and thus z can be approximated by

$$z(\theta) = z_0 - (z_0 - z_d)(\theta/\theta_d) \tag{37}$$

The relation between L, z, and θ is

$$\mathrm{d}L = z\,\mathrm{d}\theta \tag{38}$$

Combining this with Eq. (37) and integrating gives

$$L(\theta) = z_0\theta - \tfrac{1}{2}[(z_0 - z_d)/\theta_d]\theta^2 \tag{39}$$

Equation (39) matches the measured data to within 0.25%. (With a very small adjustment of z_0 and/or z_d, the formula could forecast the final deployed length perfectly.) The mass of the tether remaining on the reel during deployment is a function of the deployed length and is

$$m_t(\theta) = m_{t0} - \rho L(\theta) \tag{40}$$

The moment of inertia of the reel and tether is

$$I = I_d + I_{t0} - \tfrac{1}{2}\rho L\left(z_0^2 + z^2\right) \tag{41}$$

and thus depends on z and implicitly on θ.

Kinetics

The magnetic hysteresis brake exerts a constant retarding torque $G_{\rm mb}$ while slipping if $T_1 z \geq G_{\rm mb}$, where T_1 is the tether force and z is the radius of the reel. If $T_1 z$ falls below $G_{\rm mb}$, the brake stops slipping and holds its angular position. A torque balance during deployment (brake slipping) of the reel and rolled-on tether about the reel rotation axis results in

$$I\frac{\mathrm{d}^2\theta}{\mathrm{d}t^2} = T_1 z - G_{\rm mb} \tag{42}$$

The magnetic hysteresis clutch cannot reverse and retract the deployed tether. Thus, Eq. (42) is accompanied by the condition

$$\frac{\mathrm{d}\theta}{\mathrm{d}t} \geq 0 \tag{43}$$

Basic Model with Inextensible Tether

The basic dynamic characteristics relevant to planning and design for this category of mission can be derived with a model in which the deploying tether is inextensible (longitudinal flexibility will be discussed further in a later section). For an inextensible tether,

$$r_1(t) = L(t) \tag{44}$$

From Eq. (38),

$$\frac{\mathrm{d}L}{\mathrm{d}t} = z\frac{\mathrm{d}\theta}{\mathrm{d}t} \tag{45}$$

Because $\mathrm{d}z/\mathrm{d}t$ is very small, $\mathrm{d}^2L/\mathrm{d}t^2 \cong z\,\mathrm{d}^2\theta/\mathrm{d}t^2$. Combining this with Eq. (42) results in

$$T_1 = (I/z^2)\ddot{L} + G_{\rm mb}/z \tag{46}$$

Combine Eqs. (44) and (46) with Eq. (30a) to obtain

$$\left(1 + I\big|_{m_e z^2}\right)\ddot{L} = \left\{\left(\mu\big|_{R_{\rm cm}^3}\right)\left(3n_1^2 - 1\right) + \omega_2^2 + \omega_3^2\right\}L - G_{\rm mb}/m_e z + F_1^b\big|_{m_b} \tag{47}$$

Equation (47) is basically a force balance along the tether direction. The term on the left-hand side models the inertia of the payloads and reel to separation. The first term on the right models the gravity gradient and centrifugal forces that separate the subpayloads and is proportional to L. The second term models the separation action of the thruster on the forward subpayload. The third term models the retarding action of the magnetic hysteresis brake. For the deploying inextensible tether, Eqs. (30b) and (30c) become

$$\dot{\omega}_3 + 2(\dot{L}/L)\omega_3 + \omega_2\omega_3 \tan\delta = 3\left(\mu\big|_{R_{\rm cm}^3}\right)n_1 n_2 \tag{48}$$

$$\dot{\omega}_2 + 2(\dot{L}/L)\omega_2 - \omega_3^2 \tan\delta = 3\left(\mu\big|_{R_{\rm cm}^3}\right)n_1 n_3 \tag{49}$$

Equations (47–49), together with Eqs. (42) and (45), have been solved for various subphases of the OEDIPUS-C mission by analytic and/or numerical computer solution as described in the following sections.

Flight Data from OEDIPUS C

The phases of the mission are shown in Fig. 1. They are 1) launch, separation from launch vehicle, and attitude reorientation (t = 0–174 s); 2) initiation of deployment by thrusters (t = 0–174 s); 3) tether deployment phase, where thruster force is zero and L increases to full length (t = 174–453 s); 4) fully deployed phase (t = 453–623 s); and 5) motion of mass points after tether severance (t = 634–947 s). The tension history that was measured with a tether force sensor during the enumerated phases is shown in Fig. 6. The right ascension and declination data measured with a star camera are shown in Figs. 7 and 8. The physical parameters of OEDIPUS C are given in Table 1.

Simulation and Analysis and Comparison with Flight Data

This section presents analysis and/or simulation of each of the enumerated phases and compares results with the flight data of OEDIPUS C.

Initiation of Deployment by Thrusters

The nonlinear differential equations of the foregoing analysis are singular for $L = 0$ and are ill conditioned if L is small. The best way to deal with this problem is to use an approximate analytical solution for the initial stages of deployment. When L is small, the dominant separation force is the due to thrusters, and the gravity gradient and centrifugal forces are negligible. For small L, Eq. (47) is approximately

$$\left(1 + I\big|_{m_e z^2}\right)\ddot{L} = -G_{\rm mb}/m_e z + F_b/m_b \tag{50}$$

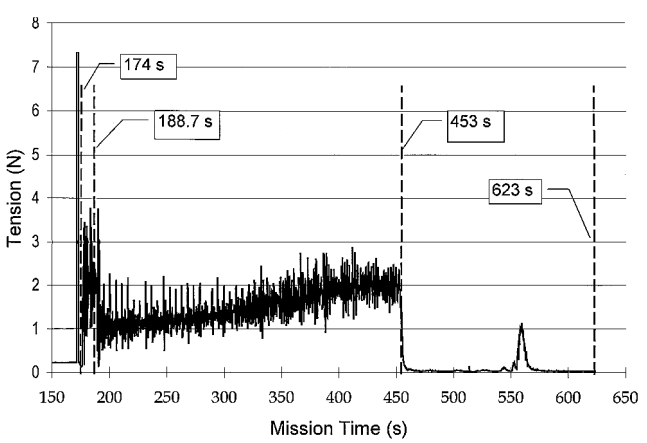

Fig. 6 Tension history, measured with OEDIPUS-C tether force sensor.

Table 1 OEDIPUS C parameters

Parameter	Symbol	Value	Unit
Gravitational constant	μ	398,601	km^3/s^2
Mass of aft payload	m_a	93.0	kg
Mass of forward payload	m_b	115.4	kg
Length of deployed tether	L_f	1,174	m
Tether mass/length	ρ	0.0027554	kg/m
Radius of undeployed tether	z_0	0.0579	m
Radius of inner spool	z_d	0.0132	m
Initial length of tether on spool	——	1,305.49	m
Number of turns of tether wire	$\theta_d/2\pi$	5,830	turns
Initial mass of tether on spool	m_{t0}	3.59236	kg
Moment of inertia of inner spool	I_d	0.0004	km-m^2
Initial inertia of tether wire	I_0	0.00631	kg-m^2
Magnetic brake torque	$G_{\rm mb}$	0.0512	N-m
Pitch of helical tether	——	0.635	m
Stiffness associated with helix	——	0.0034	N-m
Longitudinal material stiffness	EA	9,000	N
Thrust level	F_1^b	59.38	N
Time of separation	t_0	174	s
Burn time of thrust	——	14.7	s

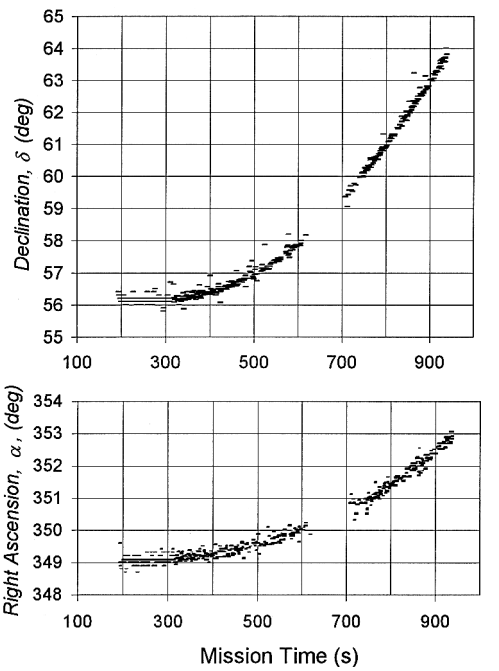

Fig. 7 Right ascension and declination history, measured with OEDIPUS-C star camera.

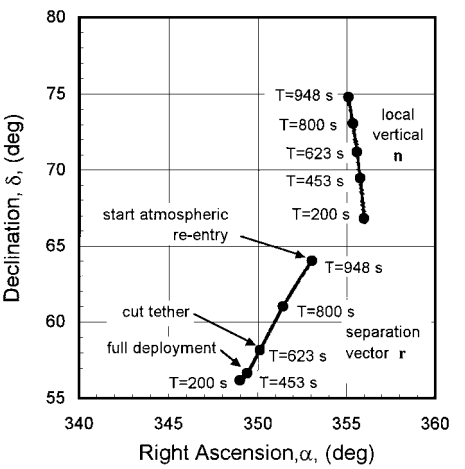

Fig. 8 Right ascension vs declination flight data.

Substitute this into Eq. (46) to obtain the tension during deployment:

$$T_1 = \frac{I}{z^2}\left(\frac{1}{1 + \left(I \middle/ m_e z^2\right)}\right)\frac{F^b}{m_b} + \frac{G_{\mathrm{mb}}}{z}\left(1 - \frac{I}{m_e z^2}\right) \tag{51}$$

Equation (51) shows that the initial tether tension is comprises two components, one due to the thruster force and the other due to the magnetic hysteresis brake. For OEDIPUS C (Table 1), $I_0/m_e z_0^2 = 0.039$, which indicates that the main inertia to separation is due to the payload masses and the reel contribution is about 3.9%. At the initiation of deployment, where $z = z_0 = 0.0579$ m, Eq. (51) yields

$$T_1 = (0.994 + 0.849)\,\mathrm{N} = 1.84\,\mathrm{N}$$

Thus, the thrusters contribute 54% of the tether tension, and the magnetic brake contributes 46%. Figure 6 shows the OEDIPUS flight data for tension vs time.[9] The data show an initial spike of up to 7.4 N and then a relaxation to near zero. Then the thrusters-on phase begins at 174 s and lasts for 14.7 s to time 188.7 s. The tension data fluctuate, likely due to the reel bearings and flexibility in the tether. The initial tension in the first 14.7 s is observed to average about 2 N, which agrees reasonably well with the calculated 1.84 N.

Equation (50) may be integrated twice to provide an expression for length vs time:

$$L(t) = \dot{L}_0(t - t_0) + \frac{1}{\left\{1 + \left(I \middle/ m_e z^2\right)\right\}}\left(\frac{F_b}{m_b} - \frac{G_{\mathrm{mb}}}{m_e z}\right)\frac{(t - t_0)^2}{2} \tag{52}$$

The radius z was assumed constant in the preceding integration. $\dot{L}_0$ is due to the separation spring [$= \sqrt{(2U_s/m_e)}$] and is very small relative to the thruster impulse for OEDIPUS C. The thrusters are turned off by onboard logic that operates from the reel encoder. The logic was set to turn off the thruster when $\dot{L}$ reached a value of 7 m/s. Flight data shows that turnoff occurred 14.7 s after payload separation, that is, at $t_1 = t_0 + 14.7$ s $= 188.7$ s. A calculation with Eq. (52) and the parameters of Table 1 yields

$$L(t_1) = 51.7\ \mathrm{m}, \qquad \dot{L}(t_1) = 7.04\ \mathrm{m/s} \tag{53}$$

Thus the OEDIPUS-C data are in accord with Eq. (52).

Deploying Phase and Deployment Termination

After thruster turnoff, $L \neq 0$ and this main phase of the deployment can be simulated using a numerical computer solution. Equations (20), (21), (45), (47), (48), and (49) are six coupled scalar differential equations in L, ω_2, ω_3, θ, α, and δ. Kinematic variables z and I, which are linked algebraically to θ, are also present in the differential equations; they can be provided for either with the detailed kinematic data of the reel or with Eqs. (37) and (41). R_{cm}, n_1, n_2, and n_3 are known input functions calculable from the trajectory. The equations were programmed for numerical solution with a Runge–Kutta integration routine using MATLAB®. This phase was simulated with $F_1^b = 0$ and the initial conditions at $t_1 = 188.7$ s. Equations (53) are the initial conditions on L and $\dot{L}$. The initial conditions for α and δ are taken from Fig. 7 and are 349 and 56.2 deg, respectively. Figure 9 gives the simulation data, where $\dot{\theta}$ and $\dot{L}$ have maxima at $t_1 = 188.7$ s and slowly decrease as deployment progresses. The termination of deployment is recognized to be the point at which $\mathrm{d}\theta/\mathrm{d}t$ reaches zero. At this point, the initial separation impulse plus a gravity gradient impulse is fully dissipated by the magnetic clutch, and $\dot{L}$ reaches zero. As the bodies have, thus, stopped moving relative to each other, the tension drops to near zero. The magnetic hysteresis brake cannot retrieve the tether and so $\mathrm{d}\theta/\mathrm{d}t$ remains at zero thereafter. The end of deployment in the simulation is at 452 s, and this compares with 453 s of the flight data (Fig. 6). Also the simulation calculates L to be 1133 m, which is within 3% of the flight data value of 1174 m. The simulation produces tensions of 0.875 and 2.21 N at the beginning and end of deployment, respectively, and this compares with average values of Fig. 6 of about 1.0 and 2.0 N.

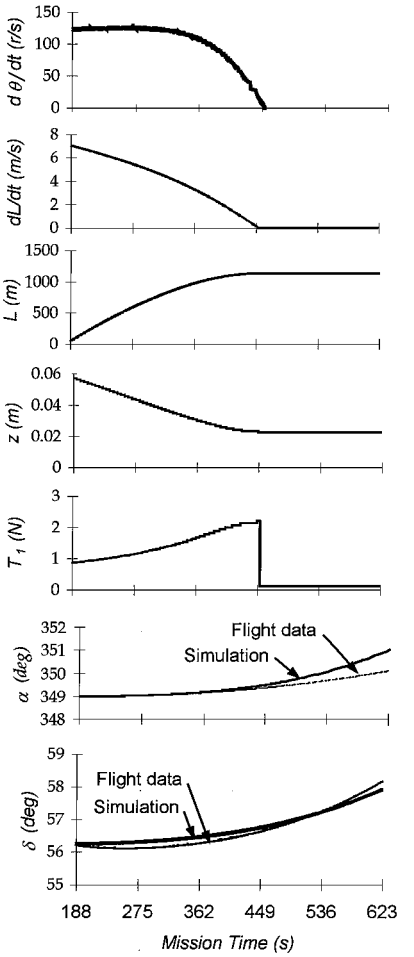

Fig. 9 Simulation results of deployment and deployment termination.

The nature of the tether deployment can be illustrated by an approximate solution of Eq. (47) in which the gravity gradient and centrifugal forces are ignored. The equation to be solved is essentially Eq. (50) with $F_1^b = 0$ and the initial conditions of Eq. (53). Integration once results in

$$\dot{L} = \dot{L}(t_1) - \frac{1}{\left\{1 + \left(I/m_e z_m^2\right)\right\}}\left(\frac{G_{\mathrm{mb}}}{z_m}\right)(t - t_1) \tag{54}$$

A second integration gives

$$L = L(t_1) + \dot{L}(t_1)(t - t_1) - \frac{1}{\left\{1 + \left(I \middle/ m_e z_m^2\right)\right\}}\left(\frac{G_{\mathrm{mb}}}{z_m}\right)\frac{(t - t_1)^2}{2} \tag{55}$$

In the preceding integration, z is approximated by a constant mean value, $z_m = (z_1 - z_f)/2$. Deployment ends where $\dot{L} = 0$ in Eq. (54). Equation (54) yields 456 s for OEDIPUS-C parameters. This is in good agreement with the flight value of 453 s (see Fig. 6). Equation (55) yields a length $L = 992$ m, which is 15% less than the flight value of 1174 m. A corresponding approximate expression for the tension in this subphase is

$$T_1 = (G_{\mathrm{mb}}/z_m)\left(1 - I \middle/ m_e z_m^2\right) \tag{56}$$

This formula yields tensions of 0.84 and 2.26 N and beginning and end of deployment, respectively. The tensions correspond to flight values (Fig. 6) of about 1.0 and 2.0 N, respectively.

Fully Deployed Phase

The reel's angular turn rate $\dot{\theta}$ and the payload separation rate $\dot{L}$ reach zero at 453 s, and this marks the end of deployment and the start of the fully deployed phase. The tension drops, and the magnetic hysteresis brake locks into one of its detent positions. If the tether were truly inextensible, the tension would drop suddenly to near zero. However, the flight data of Fig. 6 show a more complex situation, which has been investigated in Ref. 7. The flight-measured tension in this phase ($t = 453$–623 s) is noted to be very small most of the time, but in addition a tension increase/decrease is observed at about 570 s. Basically, at the end of deployment at $t = 453$ s, the tether has a longitudinal elastic stretch u due to the tension, and the separation distance r_1 is actually $L + u$. The relative payload motion stops when the reel stops, and then the elastic force causes the payloads to rebound toward each other (i.e., $u \to 0$ and $r_1 \to L$); the tension drops to near zero over a time period of several seconds. Beyond this point, the gravity gradient and centrifugal effect become dominant forces on the two end bodies. The sum of the gravity gradient and centrifugal force in the tether direction can be deduced from Eq. (30a) with $\dot{r}_1 = 0$ and $F_1^b = 0$ and is

$$N = m_e\left\{\left(\mu \middle| R_{\rm cm}^3\right)(3\cos^2\beta - 1) + \omega_2^2 + \omega_3^2\right\}r_1 \qquad (57)$$

where β is the angle between $\boldsymbol{c}_1$ and $\boldsymbol{n}$, that is, between the separation vector and the local vertical (or equivalently between $\boldsymbol{r}$ and $\boldsymbol{R}$). Also $\cos\beta = n_1$ (n_1 is also equal to $\cos\delta\cos\alpha$, which is a less convenient expression in this context).

In general, N of Eq. (57) may be positive (which would cause tension in the tether) or negative (which would cause the payloads to approach each other and the tether to become slack), depending on the value of β, ω_2, and ω_3. If ω_2 and ω_3 are negligible, then N would be positive if $3\cos^2\beta - 1 > 0$, or equivalently if $\beta < 59.7$ deg. If $\beta > 59.7$ deg, N would be negative.

The OEDIPUS-C flight data of β are evident in Fig. 8; β is the difference between the separation vector and the local vertical and is about 10–12 deg over the duration of the mission. Also the ω can be evaluated from Fig. 7 and they are found to be very small. Thus, N of Eq. (57) is positive and induces separation of the payloads and a tensioned tether. Equation (57) yields a calculated value of approximately 0.12 N, which causes the payloads to separate. The tether stretches due to flexibility contributed by a residual-stress helix in the tether (the tether is stored on the reel, and when deployed has a helical preset) and also to material flexibility EA/L. Because the induced tension in the tether is considerably less than $G_{\rm mb}/z$ of about 1 N, the magnetic hysteresis brake will remain locked. As the payloads separate, the tether stretches and resists the separation motion; the tension history in Fig. 6 shows a rises/fall at about 560 s that is indicative of the payload separation stopping and acquiring an equilibrium state.[5,7] Although these effects are sensed clearly with the tether force sensor, the associated length changes are small (about 2 m or less).

Simulation of α and δ during this phase are included in Fig. 9. The flight data of Fig. 7 are also superimposed on the simulation results. The attitude motion is noted to be small (about 1.5 deg of arc), and simulation and flight data are in accord.

Posttether Severance Phase

In the OEDIPUS-C mission, the tether was severed simultaneously at the aft and forward payloads with a guillotine-type cutter at $t_s = 623$ s. The dynamics after separation may be modeled in this phase with Eqs. (20) and (21) and Eqs. (30) with $T_1 = 0$ and $F_1^b = 0$. The initial conditions are taken from the flight data. From the flight data of Fig. 7, $r_1(t_s) = L_f = 1174$ m, $\dot{r}_1(t_s) = 0$, and $\alpha(t_s)$ and $\delta(t_s)$. Figure 10 shows the simulation result. Also the flight data for attitude is superimposed. The simulation and flight data are noted to be in accord.

An approximate analytical solution for $r_1(t)$ for this phase may be obtained from Eq. (30a):

$$\ddot{r}_1 = \left\{\left(\mu \middle| R_{\rm cm}^3\right)(3\cos^2\beta - 1) + \omega_2^2 + \omega_3^2\right\}r_1 \qquad (58)$$

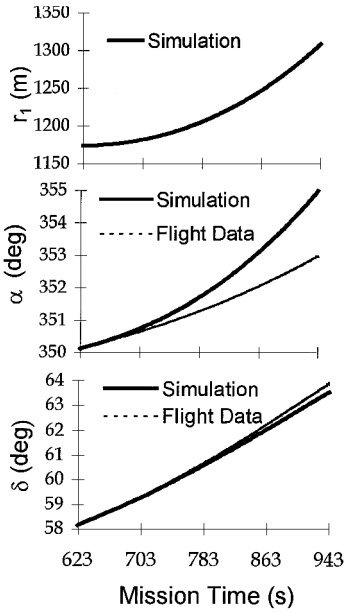

Fig. 10 Simulation vs flight data; posttether severance.

$R_{\rm cm}$, β, ω_2, and ω_3 are approximately constant during this phase. If the coefficient of r_1 is regarded as constant, the differential equation can be solved. The solution is

$$r_1(t) = Ae^{\lambda(t-t_s)} + Be^{-\lambda(t-t_s)} \qquad (59)$$

where $\lambda = [\{\mu(3\cos^2\beta - 1)/R_{\rm cm}^3\} + \omega_2^2 + \omega_3^2]^{1/2}$. With the initial conditions $r_1(t_s) = L_f$ and $\dot{r}_1(t_s) = 0$, one obtains $A = B = L_f/2$, and Eq. (59) then becomes

$$r_1(t) = L_f \cosh\lambda(t - t_s) \qquad (60)$$

Equation (60) has the shape of the simulation curve of $r_1(t)$ of Fig. 10. For OEDIPUS C, Eq. (60) yields 1302 m at $t = 943$ s (with $\beta = 10$ deg), which compares with the simulation value in Fig. 10 of 1308 m.

Conclusions

Mathematical models and simulations have been successfully developed for the deployment, postdeployment, and posttether severance phases of the OEDIPUS type of space tether mission. As well, approximate solutions of the model are obtained that lead to a functional formula that may be used in mission planning and concept design. The mathematical modeling is demonstrated to be in agreement with flight-measured tether tension and orientation data from the OEDIPUS-C mission. Although the modeling has been developed for the OEDIPUS-C type of mission, the method and basic form of equations apply more widely and may be adapted to other categories of orbital tether missions.

Acknowledgments

This work was funded by the Space Technology Branch of the Canadian Space Agency (CSA). Jennifer O'Neill, University of Waterloo, developed the computer simulation and helped to sort out computational singularities as part of a university cooperative work term while at the CSA.

References

[1]James, H. G., and Tyc, G., "Flight Results from the OEDIPUS-A Tethered Experiment," *Proceedings of the 4th International Conference on Tethers in Space*, Science and Technology Corp., Hampton, VA, 1995, pp. 193–209.

[2]Eliuk, R., Walkty, I., Rob, R., Rumbold, G., and James, H. G., "OEDIPUS-C Tethered Suborbital Mission Description and Flight Performance," *Proceedings of the 9th CASI Conference on Astronautics*, Canadian Aeronautics and Space Inst., Ottawa, ON, Canada, 1996, pp. 332–341.

[3]Raitt, W. J., "Sounding Rocket Tethered Experiments: The NASA CHARGE Program," *Proceedings of the 4th International Conference on Tethers in Space*, Science and Technology Corp., Hampton, VA, 1995, pp. 1837–1846.

[4]Jablonski, A. M., Vigneron, F. R., Tyc, G., Han, R. P. S., Misra, A. K., Modi, V. J., and Chandrashaker, R., "OEDIPUS-C Tether Dynamics Experiment," *Proceedings of the 9th CASI Conference on Astronautics*, Canadian Aeronautics and Space Inst., Ottawa, ON, Canada, 1996, pp. 18–30.

[5]Tyc, G., Vigneron, F. R., Jablonski, A. M., Han, R. P. S., Modi, V. J., and Misra, A. K., "Flight Dynamics Results from the OEDIPUS-C Mission," AIAA Paper 96-3573, July 1996.

[6]Vigneron, F. R., Jablonski, A. M., Chandrashaker, R., and Tyc, G., "Damped Gyroscopic Modes of Spinning Tethered Space Vehicles with Flexible Booms," *Journal of Spacecraft and Rockets*, Vol. 34, No. 5, 1997, pp. 662–669.

[7]Tyc, G., "Dynamics and Stability of Spinning Flexible Space Tether Systems," Ph.D. Dissertation, Dept. of Mechanical and Industrial Engineering, Univ. of Manitoba, Winnipeg, MB, Canada, May 1998.

[8]Beattie, D., Krabel, E., and Whitehead, W., "Attitude Data Reduction of the OEDIPUS-E Sounding Rocket Mission," *Proceedings of the 9th CASI Conference on Astronautics*, Canadian Aeronautics and Space Inst., Ottawa, ON, Canada, 1996, pp. 322–330.

[9]Jablonski, A. M., Vigneron, F. R., Rhew, R. D., Bergmans, J. L., Whitehead, W. R., and Tyc, G., "Preflight Testing and Flight Performance of the OEDIPUS-C Tether Force Sensor," *Journal of Spacecraft and Rockets*, Vol. 34, No. 4, 1997, pp. 533–541.

[10]Hughes, P. C., "Vectices—Appendix B," *Spacecraft Attitude Dynamics*, Wiley, New York, 1986, pp. 522–534.

[11]Likins, P. W., "Dynamics and Control of Flexible Space Vehicles," NASA TR 32-1329, Jet Propulsion Lab., California Inst. of Technology, Pasadena, CA, Feb. 1969.

F. H. Lutze Jr.
Associate Editor